SYSTEM-ON-CHIP 36.8 GHz RADIOMETER FOR SPACE-BASED OBSERVATION OF SOLAR FLARES: FEASIBILITY STUDY IN 0.25 µm SiGe BiCMOS TECHNOLOGY

L. Aluigi[1], L. Roselli[1], S. M. White[2], and F. Alimenti[1, *]

[1]Department of Electronic and Information Engineering (DIEI), University of Perugia, Via Duranti 93, Perugia 06125, Italy

[2]Space Vehicles Directorate, AFRL, Kirtland AFB 87117, USA

Abstract—This paper deals with a feasibility study for a System-on-Chip (SoC) mm-wave radiometer devoted to space-based observation of solar flares and operating in the Ka-band. The radiometer has been designed in 250 nm SiGe BiCMOS process. The circuit integrates a three stages differential LNA with 37.2 dB gain and 4.8 dB noise figure at 36.8 GHz and a differential square-law detector based on HBTs, featuring a 96 mV/µW responsivity. The full radiometer achieves, potentially, a NETD of 0.1 K for 1 s integration time in Dicke mode. This work represents the first study of such an integrated instrument for Ka-band space-based observation of solar flares.

1. INTRODUCTION

The Sun is currently running through its maximum, the phase of most intense activity which occurs once every 11 years. During this period, it erupts violently, emitting solar flares or throwing out coronal mass ejections (CMEs) consisting of billions of tons of charged particles. These events can trigger geomagnetic storms on Earth that could pose extraordinary risk to our critical systems and even our way of life [1].

As the human infrastructure has greatly expanded and grown more complex, now more than ever, it is important to study and investigate the events as solar flares in order to prevent possible risks associated with massive geomagnetic storms.

Millimeter-wave (mm-wave) radiometers are commonly employed in ground- and space-based scientific experiments ranging from the observation of the Earth's atmosphere, forest-fire detection

and oceanographic studies, to radio-astronomic experiments such as the measurement of the Cosmic Microwave Background [2–4]. Space agencies are showing a great interest in the development of miniaturized instruments in such a way as to meet the mission constraints imposed by the adoption on micro- and nano-satellites [5]. Millimeter-wave receiver front-ends for radiometric imaging are under development mainly exploiting CMOS SiGe BiCMOS or GaAs PHEMT processes [6–8]. However, the cited designs are only focused on ground-based applications such as imaging for security scanners and material analysis. In parallel, several mm-wave square-law power detectors have been published, showing that the integration of this fundamental building block is possible either with SiGe BiCMOS [9, 10] or with CMOS [11]. As a consequence of the high scientific and industrial interest around the passive mm-wave imaging, the first SoC mm-wave passive receiver on silicon has been published at the end of the year 2010 [12]. This integrated circuit is based on a 65 nm CMOS technology and exploits a direct amplification receiver. The radiometer is equipped with an on-chip square-law detector and with an input Dicke switch for the receiver calibration.

The previous survey of the state-of-the-art shows that, until today, the design of a mm-wave radiometer for space-based applications exploiting a single silicon chip, is a completely original idea. Indeed all the cited prototypes are not suited for space mainly because they do not use space-qualified processes. The space-qualification of a 250 nm SiGe BiCMOS technology, however, is currently under development by a European foundry, the IHP at Frankfurt-Oder, Germany [13].

In this paper, two very innovative concepts will be developed. First it will be shown that solar flares could be detected and measured in the mm-wave frequency range from a space-based platform [14]. This methodology has never been attempted before, and allows us to reach a sensitivity much higher than that of conventional ground-based experiments. Second, it will be demonstrated that the above observations could be carried-out with a novel instrument: a silicon System-on-Chip (SoC) mm-wave radiometer. Working with SoC instruments will significantly reduce weight, size and power consumption, all variables of extreme importance in space applications. In addition, the SoC implementation will allow unprecedented instrumental performance. One of the major technological challenges in the realization of millimeter-wave radiometers, in-fact, is the long-term stability of the receiver parameters such as, for example, the gain and the noise figure. High parametric stability can be achieved by maintaining at constant temperature a single chip of few square millimeters (the one containing the radiometer) with a remarkable

save of power consumption. This latter aspect can also solve many problems related to operational conditions of the satellites, as huge temperature variations occur during the transition from night to day along the orbital progression and significant thermal gradients within the satellite itself.

The feasibility study will be carried-out starting from the characteristics of solar flares (solar flare flux density) and will be developed by describing the miniaturized instrument at both system- and transistor-levels. The paper is organized as follows. The scientific background of solar flares observation is given in Section 2. Section 3 describes the system design details. Section 4 illustrates the building-blocks design details, while Section 5 discusses the simulated results for the designed radiometer.

2. SCIENTIFIC BACKGROUND

Solar flares are a sudden release of a great amount of energy stored as high magnetic fields in solar active regions. Lasting minutes to hours, they are sources of radiation and particles. The magnetic energy is rapidly converted into thermal, kinetic and mechanical energies and the consequence is that the local plasma is heated to several tens of millions degrees, while particles are accelerated up to high energies. Flares are unique for the diversity of emission mechanism they exhibit and the broad range of wavelengths at which they radiate: from radio-wave, millimeter-wave, soft and hard-X rays, up to γ-rays with energies reaching 1 Gev [15, 16].

Millimeter-wave observations are the most sensitive tool to study the highest energy (i.e., > 1 Mev) electrons accelerated in solar flares [17]. Fig. 1 shows the effect of MeV-energy electrons on the radio spectrum of a solar flare. The solid line is the calculated spectrum emitted by electrons in a power-law distribution of energy with spectral index -3.6, extending from 20 keV to 20 MeV in a constant magnetic field of 600 G. The dashed curve, instead, is the spectrum emitted by the same electron energy distribution but extending only from 20 to 300 keV. When the MeV-energy electrons are absent, emission at millimeter wavelengths is reduced by orders of magnitude whereas microwave emission is not greatly changed. At low frequencies discrete harmonics are seen in the model due to the unrealistic assumption of a homogeneous magnetic field in the corona.

The experimental derivation of the above graph is of paramount help to improve existing particle acceleration models, the latter constrained by limited ground based observations [18]. Dedicated observations of solar flares at millimeter-waves are needed to obtain
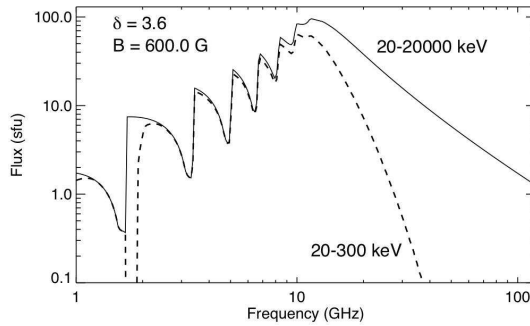
Figure 1. The effect of MeV-energy electrons on the radio spectrum of a solar flare. Only the non-thermal gyrosynchrotron radiation mechanism is considered in these simulations. The source (i.e., the flare) has a size of 3 arcseconds by 10 arcseconds on the sky, with a thickness of 1 arcsecond. These source dimensions are typical of small-sized flares.

the peak frequency and the high frequency slope of radio spectra [19], both of which are crucial to infer the energy distribution of relativistic electrons. These observations are important also to study energy transport in the corona and in the lower solar atmosphere during the extended phase of solar bursts.

Large flares in the 30–40 GHz band are often optically thick and thus of limited use for quantitative work. The present discussion, however, concerns on a 36.8 GHz radiometer for three reasons. First, a miniaturized SoC instrument can be realized with present technologies [13]. Second, assuming a space-based operation of this instrument, an unprecedented sensitivity limit can be reached, allowing for the detection of weak events. Third, the same methodology could be applied to the 90–100 GHz band as soon as space-qualified silicon SoC will be ready for that. This means, in particular, the availability of Low-Noise Amplifiers (LNA) operating at these frequencies.

During solar flares, large scale magnetic field structures can be destabilized and be propelled into the interplanetary medium, along with the large masses they contain, to form the CMEs. It is now recognized that CMEs are the principal drivers for the Space Weather and the near-Earth conditions [17]. Although the above phenomena are well documented by the available observations, they raise questions that are still unsolved. In particular, measurements from SOHO observations [20] showed a strong relationship between helioseismology and flares: global oscillations of our Star seem to be strongly correlated with solar flares. Moreover, it would also be important to understand

what physical process stands behind the heating of the solar corona.

2.1. Limitations of Ground Based Measurements

Ground based measurements are available 17, 35 and 80 GHz [21]. To improve the quantitative study of flares at these frequencies, instruments with high detection probability are needed. This can be achieved with: a good sensitivity; a large Field of View (FoV), full disk capability being optimal; a high time-on-target; and a high time resolution, the latter to capture fast time structures. From this point of view it can be noted that ground-based single-dish observations at millimeter wavelengths are limited by fluctuations in atmospheric opacity. As a consequence the sensitivity is met by reducing the FoV to a portion of the solar disk. On the other hand full disk capability is possible with nulling interferometers, such as the Nobeyama 80 GHz instrument [21], but the practical sensitivity is limited because the dishes must be small. In any case the maximum time-on-target achievable at ground is limited to about eight hours per day in good weather conditions.

The list of solar flares that have been detected at millimeter wavelengths from the ground remains small for two very good reasons: firstly, except in the largest events, millimeter emission has a spectrum that falls as frequency increases, limiting flux levels; and secondly, observations from the ground are limited by atmospheric opacity fluctuations which typically impose a detection threshold well above the instrumental noise level.

2.2. Solar Flares Spectral Flux Density

The emission captured by a radio telescope is measured in terms of the intensity I_f, which is the power received per square meter and per solid angle unit within a bandwidth of one Hz [22]. Integrating I_f over the solid angle Ω_s subtended by the emitting radio source we get a quantity, S_f called the spectral flux density:

$$S_f = \iint_{\Omega_S} I_f \cdot d\Omega \tag{1}$$

In solar radio astronomy S_f is expressed in solar flux units (acronym: sfu), 1 sfu being equal to $10^{-22}\,\mathrm{W} \cdot \mathrm{m}^{-2}\mathrm{Hz}^{-1}$. The Sun is a quite strong radio source, being a few orders of magnitude stronger that the brightest non-solar radio source in the microwave.

The spectral flux density of the Sun S_f^s can be imagined as composed by two contributions: the first related to the quiet Sun S_f^{QS}

and the second due to the radiation mechanism involved in flares S_f^F.

$$S_f^S(t) = S_f^{QS}(t) + S_f^F(t) \approx S_f^{QS} + S_f^F(t) \qquad (2)$$

The contribution associated to the quiet Sun is characterized by slow temporal variations. Measurements carried-out from an Earth location are primarily influenced by the relative distance between the Earth and the Sun. Such a distance is continuously varying with the orbital position of the Earth and thus has a periodicity of one year. Once corrected for this effect, the measurements show an even slower periodicity associated with the 11-years solar cycle. The contribution due to flares, instead, evolves very quickly in time, the typical duration of a flare event being around 10 minutes. Because of this great time-scale difference, the quiet Sun spectral flux density can be considered as a constant during a flare event, leading to the approximation of Eq. (2). As a consequence, the flare contribution can be separated from the total spectral flux density by extracting the only flux variations above the quiet Sun background. The latter can be estimated with a rather simple formula [14]:

$$S_f^{QS} = \frac{2\pi k T_S \rho_S^2}{c_0^2} f^2 \qquad (3)$$

where $k = 1.38 \times 10^{-23}$ J/K is the Boltzmann's constant, $c_0 = 3 \times 10^8$ m/s is the speed of light in a vacuum, f is the frequency of analysis, ρ_s is the angular radius of the Sun (equal to 16' or $\pi/675$ radians if seen from Earth) and T_S is the brightness temperature of the Sun, which has been estimated at various frequencies by several authors [23].

Assuming from [23] the value of $T_S = 7800$ K, we evaluated Eq. (3) at 36.8 GHz. We obtained that the quiet Sun background is about 2204 sfu while one can be interested in studying small amplitude flares, in the order of 10 sfu.

The instrument we propose in the next sections, i.e., a 36.8 GHz direct detection radiometer, is designed to reach a sensitivity more than an order of magnitude better than those reached by ground based instruments. By combining the improved sensitivity with very-high on-target time coverage, it should result in a large increase in event detections and correspondingly a much more complete picture of the millimeter wave characteristics of flares. The radiometric range shall be between 0 sfu and 10000 sfu and the radiometric resolution shall be less-or-equal than 2 sfu for 1 s integration time in at least 100 s time scale. From the flare list obtained at Nobeyama radio-observatory [24] in last years, however, fluxes over 10000 sfu at 35 GHz occur in roughly 10–20 events per solar cycle (i.e., each 11 years). Furthermore there were a

few events between 100000 and 200000 sfu (very large flares) at 35 GHz in each of the last 2 cycles. This means that the proposed space-based radiometer should have some gain adjustment mechanism in order to correctly measure large flares without compromise the instrumental sensitivity during normal operation (observation of small flares).

3. INSTRUMENT ARCHITECTURE

The schematic of the 36.8 GHz receiver is shown in Fig. 2. It is based on a direct detection architecture. The chip proposed in this paper contains the millimeter-wave radiometer module. It consists of a square-law detector preceded by a low-noise amplifier and followed by a low-frequency integrator. Although the back-end is not considered in the present study, it must be noted that one of the main advantage of silicon electronics is the possibility to integrate the mm-wave receiver together with the signal conditioning and processing electronics, A/D and even with the CPU.

The antenna module will be constituted by a single parabolic dish and by a circular corrugated feed-horn placed in the focal point of
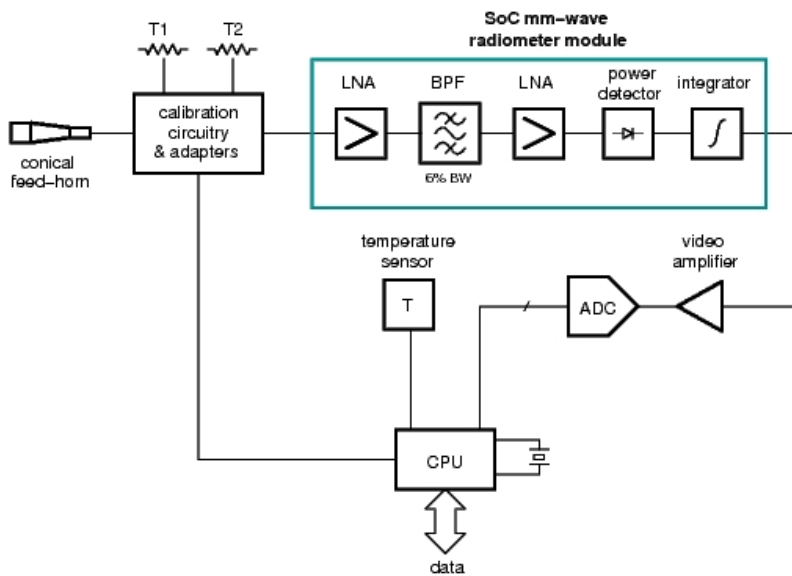
Figure 2. Schematic of the millimeter-wave radiometer module. The radiometer works in the Ka-band frequency range, centered at 36.8 GHz. A direct amplification architecture is assumed.

the dish. An offset configuration will be used in order to avoid the obstruction and scattering of the feed system. This will result in improved antenna efficiency and cross-polarization performances. The main antenna will be placed within the satellite envelope, in such a way as to reduce for temperature variations [14]. The circular corrugated horn will be connected to the receiver input by means of a waveguide adapter.

Alternative antenna configurations could be based on the quasi-optical approach as suggested in [25]. In this way a dielectric lens antenna can be combined with elementary planar radiators (like the microstrip patch) working as antenna feeds.

The antenna noise temperature T_A can be evaluated in terms of system parameters by using the following formula [26]:

$$T_A \approx \frac{\pi}{1.13} \left(\frac{\rho_S}{\Theta_h} \right)^2 T_S \qquad (4)$$

where Θ_h is the half power beam width of the antenna and ρ_s the angular radius of the Sun. The formula (4) means that the antenna temperature can be obtained as the brightness temperature of the source multiplied by the filling factor, i.e., the portion of the antenna solid angle filled by the source itself. If we consider the values given in Table 1 for the quiet sun we obtain, at 36.8 GHz, a value of T_A^{QS} equal to 1542 K.

The parabolic dish size can be estimated from the half-power beam width as in [27, p. 40]. For 1 degree at 36.8 GHz one obtains a diameter in the order of 60 cm. The SoC mmw radiometer module boosts the received signal directly at 36.8 GHz. In addition the band pass filtering and the detection is carried-out directly at the operating frequency. Once detected, the signal will be adjusted in level exploiting low-drift instrumentation amplifiers and then passed to the back-end module.

The receiver gain is determined by selecting a suitable power level P_D at the square-law detector input:

$$P_D = k \left(T_A + T_R \right) BG \qquad (5)$$

where B and G are the pre-detection bandwidth and gain respectively, while T_R is the receiver noise temperature. Assuming the linearity, the

Table 1. Antenna noise temperature.

T_S [K]	ρ_s [arcmin]	D [cm]	Θ_h [arcmin]	T_A^{QS} [K]
7800	16	60	60	1542

voltage at the detector output will be:

$$V_D = \Re P_D \tag{6}$$

$\Re$ being the detector responsivity, expressed in V/W. Combining (6) with (5), the antenna noise temperature can be related with the output radiometer voltage:

$$V_D = kBG\Re (T_A + T_R) \tag{7}$$

Such a relationship is an important link between the quantity to be measured, T_A, and the quantity effectively treated, V_D. In particular $kBG\Re$ plays the role of a temperature-to-voltage conversion constant, T_A is the wanted signal while T_R constitute the radiometric offset.

4. CIRCUIT DESIGN

The feasibility study is now carried-out at transistor level. A 250 nm SiGe BiCMOS technology, developed at the IHP foundry, is exploited for the circuits design. This process allows for 3 metal layers and thick metals option on M4 and M5. The last metallization level has a thickness of 3 μm and is well suited to the production of spiral inductors with good quality factor and planar transmission lines. The process provides a series of npn-HBT transistors characterized by $f_t = 180$ GHz and $f_{max} = 220$ GHz. The open-base breakdown voltage BVCEO is 1.9 V. In addition there are n-MOS and p-MOS transistors, Schottky diodes and MIM capacitors. Because of the high input frequency, it was not possible to obtain the required sub-nH inductances from the inductors available in the design-kit library. Thanks to the use of an automatic procedure purposely developed [28], we were able to easily generate a custom inductors library in the required range of values. This means that, in the following circuit designs all the integrated inductors and transformers have been considered with their rigorous electromagnetic models. In particular Q-factors and self-resonant frequencies have been accurately described.

4.1. Square Law Power Detector

The schematic of the designed HBTs detector is shown in Fig. 3. It is a full differential architecture composed by coupled common emitter transistors forming the detector and by a dummy detector in perfect layout symmetry. The dummy detector provides an output reference voltage for the main detector output to be used with a differential post-amplifier. The transistors dimensions and their quiescent point are selected in such a way to optimize the performances.

The HBTs are biased through a resistive network and the signal is applied differentially to the bases of $Q_{1,2}$. The DC output voltage is taken at the common collector point. Assuming a sinusoidal input signal with frequency f and amplitude V_i, the DC output voltage can be approximated by [29]:

$$V_{OUT}^{DC} \approx I_{DC} R_v \frac{V_i^2}{V_T^2} \qquad (8)$$

where I_{DC} is the DC bias current in each branch and V_T the thermal voltage.

The standard detector figure of merit is the Noise-Equivalent Power (NEP). For a given bandwidth, it is given by the detector output rms noise voltage v_n^{RMS} divided by its responsivity $\Re$, e.g.,

$$NEP_D = \frac{v_n^{RMS}}{\Re} = \frac{v_n^{RMS}}{\partial V_{OUT}^{DC}/\partial P_{IN}^{RF}} = \frac{v_n^{RMS}}{V_{OUT}^{DC}/P_{IN}^{RF}} \qquad (9)$$

where the last equality is valid only when the input signal is small enough, and the transistors can be linearized around the operating point. NEP_D is expressed in W/$\sqrt{\text{Hz}}$.

For the simulations of responsivity and NEP we used the *Harmonic Balance* solver in ADS, assuming a noise measurement band of 1 Hz [30]. Fig. 4 shows the results at 36.8 GHz and -32 dBm input power. In these conditions the detector responsivity is 96 mV/µW, while its NEP is 4.3 pW/$\sqrt{\text{Hz}}$ at 10 kHz. Table 2 summarizes the obtained values for the output noise and NEP. The circuit consumes 3.75 mW from 2.5 V. Note that the detector in Fig. 3, although independently developed, is similar to that in [10]. Furthermore, considering the scaling in both frequency and technology, also the simulated performances are comparable.

Note that the $1/f$ noise behavior reported in Fig. 4(b) is well approximated by:

$$v_n^{RMS}(f) = \frac{k_f}{\sqrt{f}} + k_w \qquad (10)$$

Table 2. Simulated output noise and NEP for the detector at -32 dBm input power.

Post Detection Frequency [Hz]	Output Noise [µV/$\sqrt{\text{Hz}}$]	NEP @ 36.8 GHz [pW/$\sqrt{\text{Hz}}$]
10000	0.42	4.3
1000	0.79	8.2
100	2	20.3
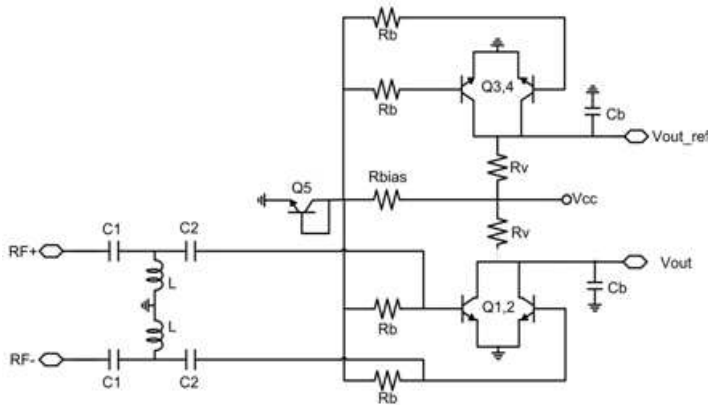
Figure 3. Schematic of the HBTs differential detector. The circuit parameters are: $Ae1 = Ae2 = Ae3 = Ae4 = 0.3\,\mu m^2$, $Ae5 = 0.15\,\mu m^2$, $L = 350\,pH$, $C1 = 38\,fF$, $C2 = 0.75\,pF$, $Cb = 1\,pF$, $Rv = 3.67\,k\Omega$, $Rbias = 10\,k\Omega$, $Rb = 1\,k\Omega$.
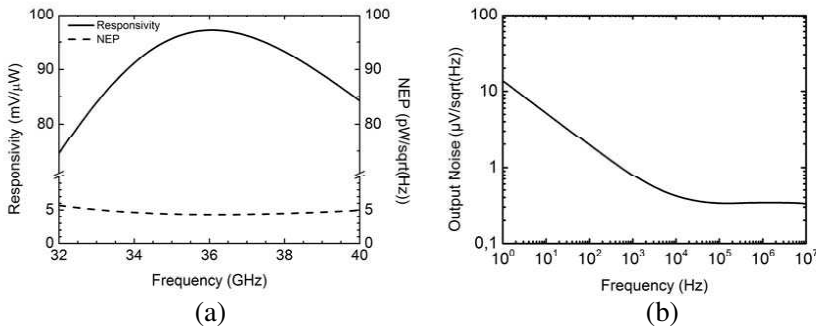

Figure 4. Simulated results for the HBTs differential detector. (a) Responsivity and NEP versus frequency at $-32\,dBm$ input power and $10\,kHz$ post detection frequency. (b) Output noise versus post-detection frequency at $36.8\,GHz$ input frequency.

where $v_n^{RMS}(f)$ is the rms voltage spectral density expressed in $V/\sqrt{Hz}$, $k_f = 1.4 \times 10^{-5}\,V$ and $k_w = 3.4 \times 10^{-7}\,V/\sqrt{Hz}$.

4.2. Low-noise Amplifier (LNA)

The differential LNA is shown in Fig. 5. It employs three stages, i.e., a first single-ended cascode stage followed by two differential cascode stages. The cascode topology allows for good stability and

(a) (b)
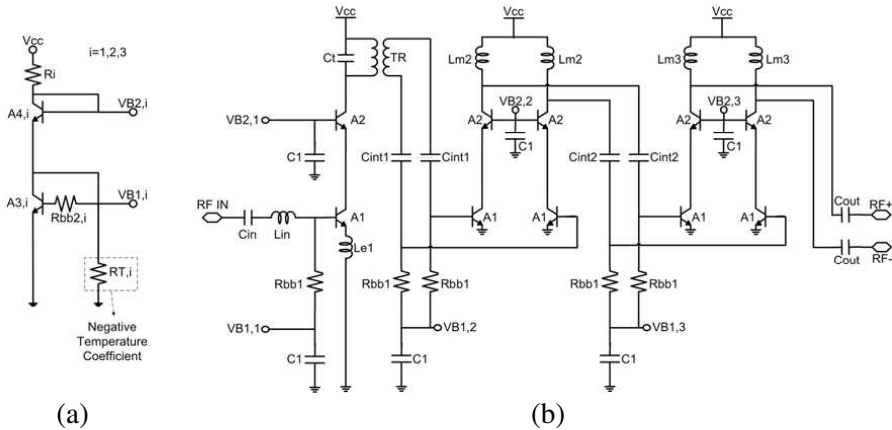
Figure 5. (a) Schematic of the LNA bias circuit. The circuit parameters are: $A3, 1 = A4, 1 = 0.15\,\mu\text{m}^2$, $A3, 2 = A4, 2 = A3, 3 = A4, 3 = 0.3\,\mu\text{m}^2$, $R1 = 0.9\,\text{k}\Omega$, $R2 = 0.4\,\text{k}\Omega$, $R3 = 0.24\,\text{k}\Omega$, $RT, 1 \rightarrow \infty$, $RT, 2 \rightarrow \infty$, $RT, 3 = 0.25\,\text{k}\Omega$, $Rbb2, 1 = 6.2\,\text{k}\Omega$, $Rbb2, 2 = Rbb2, 3 = 3.1\,\text{k}\Omega$. (b) Complete LNA schematic. The circuit parameters are: $A1 = A2 = 1.51\,\mu\text{m}^2$, $C1 = 1\,\text{pF}$, $Rbb1 = 620\,\Omega$, $Cin = 0.29\,\text{pF}$, $Lin = 200\,\text{pH}$, $Le1 = 100\,\text{pH}$, $Ct = 54\,\text{fF}$, TR is a $1:2$ step-up transformer with $K = 0.52$ and $M = 110\,\text{pH}$, $Cint1 = 46\,\text{fF}$, $Lm2 = 250\,\text{pH}$, $Cint2 = 440\,\text{fF}$, $Lm3 = 250\,\text{pH}$, Cout=45 fF.

excellent reverse isolation, which is especially important in direct-detection architectures. The first stage is optimized for low-noise operation, therefore the transistors are biased around minimum NF current density. The other stages are optimized for high-gain, therefore the transistors are biased at the maximum f_T current density [31].

For simultaneous noise and input power matching, we used a well-known LNA design procedure that takes advantage of the scalability of the devices. The transistor size (emitter length, le with a given emitter width) is chosen for the optimal noise resistance R_{OPT} to be $50\,\Omega$ at the optimal current density. Then, the degeneration inductor (L_E) increases the input resistance (R_{IN}) to $50\,\Omega$. Finally the base inductor L_{IN} matches the input reactance X_{IN}. The inter-stage matching network is designed for maximum power transfer. To have better tolerance robustness against process variations, we employed LC ladders.

Since radiometers for space applications need a very stable gain with respect to temperature, the base bias circuits are designed to compensate for the temperature variations of the LNA. The task of
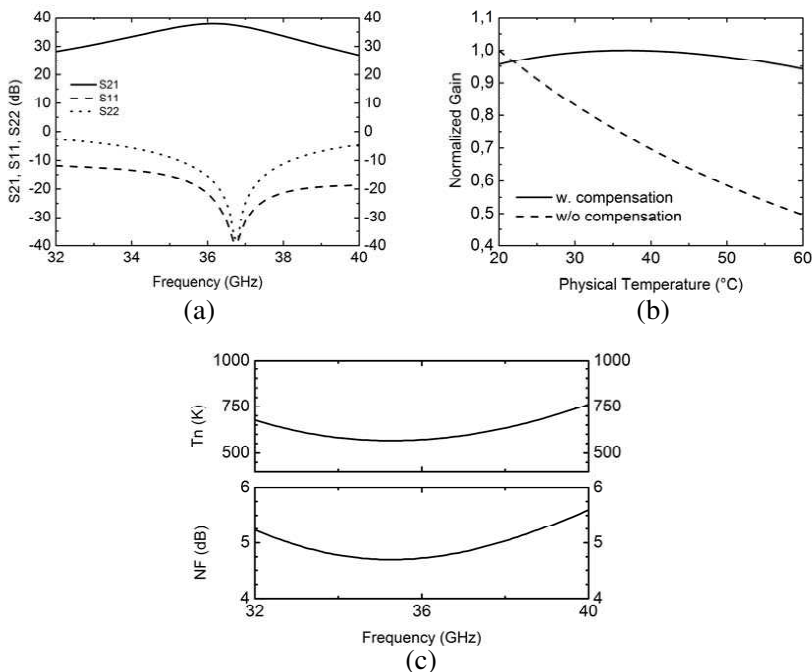
Figure 6. Circuit simulations of the LNA: (a) scattering parameters; (b) normalized gain variations versus physical temperature at 36.8 GHz; (c) noise figure and noise equivalent temperature.

the bias networks is to slightly vary the quiescent current as a function of temperature in order to keep the gain constant. To this purpose we designed a modified cascode current mirror as bias circuitry. We used a resistor with a negative temperature coefficient (R_t in Fig. 5), available in the selected BiCMOS process. R_t tends to cancel the emitter current increase, due to local temperature rise, bypassing to ground the additional base current which must be present to supply this extra emitter current [32].

The simulated S_{21}, S_{11} and S_{22} of the amplifier are shown in Fig. 6(a). At 36.8 GHz the conversion gain is 37.2 dB and the NF is 4.8 dB. The S_{11} is < -40 dB and the S_{22} is < -39 dB around the center frequency. The power consumption is 75 mW.

As mentioned above, the amplifier has also been optimized for gain stability over temperature changes, as shown in Fig. 6(b). This result is obtained accounting for the temperature drift of all transistors and resistors in the circuit. The gain stability is within 0.2 dB from

10°C to 60°C. To the authors' best knowledge this is the first time that temperature compensation techniques are applied to stabilize the gain variations of a silicon radiometer. Fig. 6(c) shows the simulated NF and the corresponding equivalent noise temperature.

5. RADIOMETER RESOLUTION AND CALIBRATION

The resolution of a millimeter-wave radiometer is defined as the standard deviation ΔT of the measured antenna noise temperature [33, 34]. The resolution formula is:

$$\Delta T = \alpha(T_A + T_R)\sqrt{\frac{1}{B\tau} + \left[\frac{NEP_D}{k(T_A + T_R)BG\sqrt{2\tau}}\right]^2 + \left(\frac{\triangle G}{G}\right)^2} \quad (11)$$

where T_A is the antenna noise temperature, T_R the receiver equivalent noise temperature, B the pre-detection bandwidth, G the receiver's gain, τ the integration time, k the Boltzmann constant, $\Delta G/G$ the gain stability of the radiometer, and α a factor equal to 1 for total-power radiometers and equal to 2 for Dicke radiometers. The importance of this expression is that it establishes a link between the standard deviation of the measured data and the main instrument parameters. T_R can be related to the receiver noise figure F_R by:

$$T_R = (F_R - 1)T_0 \quad (12)$$

$T_0 = 290\,\text{K}$ being the standard IEEE temperature at which the noise figure is defined. In order to convert a resolution ΔT expressed in terms of antenna noise temperature into a resolution ΔS_f given in solar flux units, the approach proposed in [27] is used:

$$\triangle S_f = \frac{S_f^{QS}}{T_A^{QS}}\triangle T \quad (13)$$

When the antenna is pointed toward the solar center, S_f^{QS} and T_A can be approximated by Eqs. (3) and (4) respectively. Inserting Eq. (11) into (13) one obtains:

$$\triangle S_f = \alpha S_f^{QS}\left(1 + \frac{T_R}{T_A^{QS}}\right)\sqrt{\frac{1}{B\tau} + \left[\frac{NEP_D}{k\left(T_A^{QS} + T_R\right)BG\sqrt{2\tau}}\right]^2 + \left(\frac{\triangle G}{G}\right)^2}$$

$$(14)$$

In order to estimate the radiometer resolution ΔS_f starting from the simulated circuit performances, two different cases are considered. In the first case a Dicke calibration circuit is assumed. To this purpose

the radiometer input is periodically switched between the antenna at temperature T_A^{QS} and a black-body (or a reference noise source) at temperature T_1. At the same time the detector output is multiplied by ± 1 in synchronism with the receiver input switching (lock-in amplifier). If the switching frequency f_m is sufficiently high ($f_m \gg 1/2\tau$) and $T_1 \sim T_A^{QS}$ (same order of magnitude) the gain fluctuations $\Delta G/G$ can be neglected in (14) and the resolution obtained as [4]:

$$\triangle S_f = 2S_f^{QS}\left(1+\frac{T_R}{T_A^{QS}}\right)\sqrt{\frac{1}{B\tau}+\left[\frac{NEP_D(f_m)}{k\left(T_A^{QS}+T_R\right)BG\sqrt{2\tau}}\right]^2} \qquad (15)$$

The main advantage of the Dicke configuration is that the $1/f$ noise spectrum at the detector output is modulated around $\pm f_m$ (and its harmonics). As a consequence the noise contribution within the integrator bandwidth is significantly reduced. This effect is approximated in (15) by considering the detector NFP_D at f_m. The main disadvantage, instead, is that the scene is observed for only half of the operating time. Thus, the resolution of a Dicke radiometer is only half of that shown by an ideal radiometer (with the same B and τ parameters). This is accounted for in Eq. (15) assuming $\alpha = 2$.

A total power radiometer (TPR) architecture can be used to circumvent this problem and will be considered as the second case-of-study. In order to determine the detector NEP_D, however, some further considerations are needed. The starting point is an historical work by Hersman and Poe [33], where the low-frequency behavior of a TPR instrument is studied in depth. In particular the TPR is modeled along with the calibration process. This process consists of periodically switching the receiver input on two loads at different temperatures, namely T_1 and T_2 with $T_1 < T_A < T_2$. In this way the unknown receiver gain constant ($kBG\mathfrak{R}$) and its equivalent noise temperature (T_R) can be determined and then used, in the time interval between two calibrations, to relate the output voltage to the input antenna noise temperature, as in Eq. (7). One of the main conclusions reported in [33] is that the combined action of such a calibration process and of the radiometer integrator is equivalent to a low-frequency band-pass filter. The frequency response of this filter depends on both the calibration period t_c and the integration time τ and can approximated by:

$$|H(f)|^2 = \begin{cases} 0 & f < f_L \\ 2 & f_L < f < f_H \\ 0 & f > f_H \end{cases} \qquad (16)$$

where $f_L \approx 1/2t_c$, $f_H \approx 1/2\tau$, $\tau \ll t_c$. In particular (16) neglects the frequency roll-off below f_L and above f_H since these follow the

$1/f^2$ law. Furthermore assume that the same integration time τ is used during calibration and during measurement phases. The output detector noise voltage can be computed by solving the following integral:

$$\overline{\triangle v_n^2} = \int_0^\infty \overline{v_n^2}(f) \cdot |H(f)|^2 df = 2\int_{f_L}^{f_H} \left(\frac{k_f^2}{f} + k_w^2 \right) df$$

$$= 2k_w^2 (f_H - f_L) + 2k_f^2 \ln \frac{f_H}{f_L} \tag{17}$$

Observing now that $f_H - f_L \approx f_H$, $f_L \approx 1/2t_c$, and $f_H \approx 1/2\tau$ one gets:

$$\mathrm{v}_n^{RMS} = \sqrt{\overline{\triangle v^2}} \approx \frac{k_w}{\sqrt{\tau}} + k_f \sqrt{2\ln\left(\frac{t_c}{\tau}\right)} \tag{18}$$

This detector noise voltage can thus be associated to an equivalent uncertainty ΔT_D of the input antenna noise temperature:

$$\Re kB \triangle T_D = \frac{k_w}{\sqrt{\tau}} + k_f \sqrt{2\ln\left(\frac{t_c}{\tau}\right)} \tag{19}$$

thus:

$$\triangle T_D = \frac{\frac{k_w}{\sqrt{\tau}} + k_f \sqrt{2\ln\left(\frac{t_c}{\tau}\right)}}{\Re} \frac{1}{kB} = \frac{NEP_D^{TPR}}{kB\sqrt{2\tau}} \tag{20}$$

where NEP_D^{TPR} is the detector noise equivalent power in the case of a TPR architecture:

$$NEP_D^{TPR} = \frac{\sqrt{2}k_w + 2k_f \sqrt{\tau \ln\left(\frac{t_c}{\tau}\right)}}{\Re} \tag{21}$$

The consequence of (21) is that the resolution of a TPR can be rigorously computed exploiting (14) with $\alpha = 1$ and with $NEP_D = NEP_D^{TPR}$.

The developed models (15) and (14), (21) can now be used to investigate the radiometer performances in the case of Dicke and total-power architectures. To this purpose the system parameters reported in Table 3 are considered.

These parameters are in agreement with the previous discussion about the observed source (i.e., the Sun) and the proposed circuitry (i.e., the transistor-level simulations). In particular a 0.7 dB loss has been considered between the antenna and the SoC front-end to account for the presence of the calibration circuitry. As a result the receiver noise figure (F_R) has been increased of 0.7 dB with respect to the

Table 3. System parameters.

f [GHz]	S_f^{QS} [sfu]	T_A^{QS} [K]	F_R [dB]	T_R [K]	B [GHz]	G [dB]	τ [s]	k_f [V]	k_W [V/$\sqrt{\text{Hz}}$]	$\Delta G/G$ [ppm]
36.8	2204	1542	5.5	740	2	36.5	0.01–1	1.4×10^{-5}	3.4×10^{-7}	100
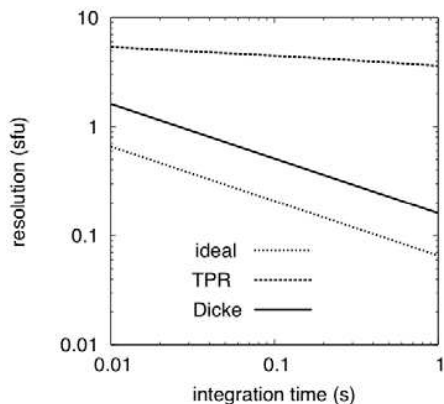
Figure 7. Radiometer resolution in sfu versus the integration time. An ideal radiometer is compared with a Dicke architecture ($f_m = 1\,\text{kHz}$, $T1 \approx T_A^{QS}$) and with TPR instrument ($t_c = 100\,\text{s}$).

simulated value at 36.8 GHz. Similarly the pre-detection gain G is decreased by 0.7 dB.

The simulated radiometer resolution in sfu is shown in Fig. 7 for both the Dicke and the TPR architectures. In the Dicke case a switching frequency $f_m = 1\,\text{kHz}$ is considered along with a reference temperature $T_1 \approx T_A^{QS}$. For the TPR architecture, instead, the two loads calibration is repeated with a period $t_c = 100\,\text{s}$, while a gain stability $\Delta G/G = 100\,\text{ppm}$ is assumed. Note that such a 100 ppm value is ten times larger than that is presently considered the state-of-the-art [35]. Finally the two above cases are compared with an ideal radiometer, the resolution of which is given by (14) for $\alpha = 1$ and $NEP_D = \Delta G/G = 0$.

From the analysis of Fig. 7 emerges that the detector noise has a significant impact on the resolution for the TPR architecture. This noise limits the instrument resolution to about 4 sfu with $\tau = 1\,\text{s}$, a value slightly higher that what is required for the observation of small flares. A more favorable situation, however, is obtained with the adoption of the Dicke configuration. In this case the resolution is well

Table 4. SoC radiometer performances for $T_A = T_A^{QS} = 1542\,\text{K}$.

	ΔS_f [sfu]	ΔT [K]
TPR architecture	5.4 to 3.6	3.8 to 2.5
($t_c = 100\,\text{s}$, $\Delta G/G = 100\,\text{ppm}$)	($\tau = 0.01\text{–}1\,\text{s}$)	($\tau = 0.01\text{–}1\,\text{s}$)
Dicke architecture	1.6 to 0.16	1.1 to 0.1
($f_m = 1\,\text{kHz}$)	($\tau = 0.01\text{–}1\,\text{s}$)	($\tau = 0.01\text{–}1\,\text{s}$)

below the 2 sfu limit for τ between 10 ms and 1 s. Such a resolution makes it possible the detection of small flares and, with $\tau = 10$ ms, also of fast time structures in the flares behavior. The achievable SoC radiometer performances are summarized in Table 4, according to the simulation study discussed throughout the paper.

6. CONCLUSION

This paper shows, for the first time, that the detection of solar flares, with unprecedented resolution and accuracy, can be effectively carried-out by means of a space-based experiment exploiting silicon SoC (i.e., ultra-miniaturized) mm-wave radiometers. To this purpose a study of the mm-wave emission of the Sun (also in the presence of a flare) has been combined with a transistor-level modeling of the main radiometer building blocks (power detector and LNAs). In particular the 250 nm SiGe BiCMOS technology from the IHP foundry has been considered as the case of study, this because the space qualification of the SG25H1 process is currently under development.

The designed SoC radiometer integrates a 3-stages LNA with a fully differential square-law power detector. The LNA features a 37 dB gain and a 4.8 dB noise figure at 36.8 GHz, whereas the pre-detection bandwidth is close to 2 GHz. Furthermore the LNA gain variations with respect to physical temperature have been significantly reduced by proposing, for the first time, a temperature compensated bias circuitry. The detector is characterized by a 96 mV/μW responsivity at −32 dBm input level and by a NEP ≈ 8.2 pW/$\sqrt{\text{kHz}}$ at 1 kHz frequency offset.

The radiometer resolution has been finally simulated accounting for both the Sun characteristics and the developed transistor-level models. It has been shown that the resolution is strictly related to the adopted calibration strategy and two cases-of-study have been considered, namely: the Dicke and the total-power architectures. From these simulations emerge that, a resolution better than 1.6 sfu is possible for an integration time of 10 ms if the Dicke approach is

adopted.

This means that the proposed SoC radiometer will be able to detect small flares (about ten times smaller than that are commonly detected with ground-based apparatuses) and to eventually reveal the presence of fast time structures. Until today, a SoC radiometer for the space-based detection of solar flares has never been proposed. This approach allows, in perspective, a number of innovations (on-chip calibration circuitry, thermal stabilization, system on-chip video amplifier, on-chip A/D converter integrated with the receiver, etc.) that will revolutionize the field of mm-wave radiometry for space-based applications.

ACKNOWLEDGMENT

REFERENCES

1. Kappenman, J., "A perfect storm of planetary proportions," *IEEE Spectrum*, Vol. 49, No. 2, 26–31, 2012.
2. Aja, B., E. Artal, L. De La Fuente, J. P. Pascual, A. Mediavilla, N. Roddis, D. Kettle, W. F. Winder, L. P. Cara, and P. De Paco, "Very low-noise differential radiometer at 30 GHz for the PLANCK LFI," *IEEE Trans. MTT*, Vol. 53, No. 6, 2050–2062, 2005.
3. Bonafoni, S., F. Alimenti, G. Angelucci, and G. Tasselli, "Microwave radiometry imaging for forest fire detection: A simulation study," *Progress In Electromegnetic Research*, Vol. 112, 77–92, 2011.
4. Joardar, S., S. Bhattacharyya, A. B. Bhattacharyya, and C. R. Datta, "Radio astronomy and super-synthesis: A survey," *Progress In Electromagnetic Research B*, Vol. 22, 73–102, 2010.
5. Aluigi, L., F. Alimenti, and L. Roselli, "Fully integrated millimeter-wave radiometers: Development level and perspectives," *Proceedings of the IEEE RAWCON*, 1–4, New Orleans, LA, 2010.
6. May, J. W. and G. M. Rebeiz, "Design and characterization of W-band SiGe RFICs for passive millimeter-wave imaging," *IEEE Trans. MTT*, Vol. 58, No. 5, 1420–1430, 2010.

7. Zito, D. and A. Fonte, "Dual-input pseudo-switch RF low noise amplifier," *IEEE Transaction on Circuit ans Systems-II: Express Brief*, Vol. 57, No. 9, 661–665, 2010.

8. Yang, M.-H., F.-H. Guan, J. Xu, X. Shi, and X.-W. Sun, "Signal model analysis of a 35 GHz alternating current direct detection receiver," *Progress In Electromagnetic Research*, Vol. 88, 275–287, 2008.

9. Rassel, R. M., J. B. Johnson, B. A. Orner, S. K. Reynolds, M. E. Dahlstrom, J. S. Rascoe, A. J. Joseph, B. P. Gaucher, J. S. Dunn, and S. A. Onge, "Schottky barrier diodes for millimeter wave SiGe BiCMOS applications," *Proceedings of IEEE BCTM*, 1–4, Monterey, CA, 2006.

10. Dacquay, E., A. Tomkins, K. H. K. Yau, E. Laskin, P. Chevalier, A. Chantre, B. Sautreuil, and S. P. Voinigescu, "D-band total power radiometer performance optimization in an SiGe HBT technology," *IEEE Trans. MTT*, Vol. 60, No. 3, 813–826, 2012.

11. Alimenti, F., S. Leone, G. Tasselli, V. Palazzari, and D. Zito, "IF amplifier section in 90 nm CMOS technology for SoC microwave radiometers," *IEEE MWCL*, Vol. 19, No. 11, 731–733, 2009.

12. Tomkins, A., P. Garcia, and S. P. Voinigescu, "A passive W-band imaging receiver in 65-nm bulk CMOS," *IEEE JSSC*, Vol. 45, No. 10, 1981–1991, 2010.

13. Microelectronics for Aerospace, Innovations for High Performance microelectronics (IHP) Frankfurt Oder, Germany. Available: http://www.ihp-microelectronics.com/en/solutions/aerospace.html.

14. Berrilli, F., A. Bigazzi, L. Roselli, P. Sabatini, M. Velli, F. Alimenti, F. Cavallini, V. Greco, P. F. Moretti, S. Orsini, M. Romoli, and S. M. White, "The ADAHELI solar mission: Investigating the structure of Sun's lower atmosphere," *Advances in Space Research*, Vol. 45, No. 10, 1191–1202, 2010.

15. Raulin, J. P., S. M. White, M. R. Kundu, A. V. R. Silva, and K. Shibasaki, "Multiple components in the millimeter emission of a solar flare," *Astrophysical Journal*, Vol. 522, No. 1, 547–558, 1999.

16. Luthi, T., "Solar flares at millimeter and submillimeter wavelengths instrumental techniques and observations," Ph.D. Dissertation, University of Bern, Bern, Switzerland, Apr. 2004.

17. Raulin, J. P. and A. A. Pacini, "Solar radio emission," *Advances in Space Research*, Vol. 35, No. 5, 739–754, 2005.

18. Miller, J. A., P. J. Cargill, A. G. Emslie, G. D. Holman,

B. R. Dennis, T. N. La-Rosa, R. M. Winglee, S. G. Benka, and S. Tsuneta, "Critical issues for understanding particle acceleration in impulsive solar flare," *Journal of Geophysical Research*, Vol. 102, No. A7, 14631–14659, 1997.

19. De Castro, C. G. G., P. Kaufmann, and J. P. Raulin, "Recent results on solar activity at sub-millimeter wavelengths," *Advances in Space Research*, Vol. 35, No. 10, 1769–1773, 2005.

20. Karoff, C. and H. Kjeldsen, "Evidence that solar flares drive the global oscillations in the sun," *The Astrophysical Journal Letters*, No. 678, L73–L76, 2008.

21. Nakajima, H., H. Sekiguchi, M. Sawa, K. Kai, S. Kawashima, T. Kosugi, N. Shibuya, N. Shinohara, and Y. Shiomi, "The radiometer and polarimeter at 80, 35 and 17 GHz for solar observations at Nobeyama," *Publ. of the Astronomic Society of Japan*, Vol. 37, 163–170, 1985.

22. Kraus, J. D., *Radio Astronomy*, McGraw-Hill, New York, 1966.

23. Solar radio astronomy at Metsähovi, Metsähovi Radio Observatory, Finland, 2008, Available: http://kurp-www.hut.fi/sun/metsahoviaurinko.shtml.

24. NoRP, the Nobeyama Radio Polarimeter, Nobeyama Radio Observatory, Japan, 2008, Available: http://solar.nro.nao.ac.jp.

25. Kim, W. G., N.-W. Moon, J.-M. Kang, and Y.-H. Kim, "Loss measuring of large aperture quasi-optics for w-band imaging radiometer system," *Progress In Electromagnetic Research*, Vol. 125, 295–309, 2012.

26. Alimenti, F, V. Palazzari, A. Battistini, L. Roselli, S. M. White, M. Velli, A. Bigazzi, and F. Berrilli, "MIOS: The ADAHELI millimeter-wave instrument for the observation of the sun," *5th ESA Workshop on Millimetre Wave Technology and Applications*, Noordwijk, NL, 2009.

27. Lüthi, T. "Nulling interferometer zur Beobachtung von Sonneneruptionen bei 90 GHz," Master Thesis, University of Bern, Bern, Switzerland, 1999.

28. Aluigi, L., F. Alimenti, and L. Roselli, "Automatic design and 3D electromagnetic simulation of sub-nH spiral inductors," *PIERS Proceedings*, 1719–1722, Marrakesh, Morocco, Mar. 20–23, 2011.

29. Zheng, L., L. Gilreath, V. Jain, and P. Heydari, "Design and analysis of a W-Band detector in 0.18-μm SiGe BiCMOS," *IEEE SiRF*, 196–199, New Orleans, LA, 2010.

30. Giambuzzi, G., "Progetto di un rilevatore di Potenza in tecnologia SiGe BiCMOS per applicazioni radiometriche a 31.4 GHz," Master

Thesis, University of Perugia, Perugia, Italy, 2011.

31. Aluigi, L., F. Alimenti, and L. Roselli, "Design of a Ka-band LNA for SoC space-based millimeter-wave radiometers," *IEEE MTT-S IMWS*, Barcelona, Spain, 2011.

32. Navon, D. H., "Technique for thermal stabilization of transistors," *IEEE Transactions on Electron Devices*, Vol. 20, No. 10, 907–909, 1973.

33. Hersman, M. H. and G. A. Poe, "Sensitivity of the total power radiometer with periodic absolute calibration," *IEEE Trans. MTT*, Vol. 29, No. 1, 32–40, 1981.

34. Lynch, J. J., H. P. Moyer, J. H. Schaffner, Y. Royter, M. Sokolich, B. Hughes, Y. J. Yoon, and J. N. Schulman, "Passive millimeter-wave imaging module with preamplified zero-bias detection," *IEEE Trans. MTT*, Vol. 56, No. 7, 1592–1600, 2008.

35. Tanner, A. B., "A high stability ka-band radiometer for tropospheric water vapor measurements," *IEEE Aerospace Conference*, 1849–1863, 2001.